PAPER

Revealing the spin-polarized optical properties of monoclinic α-Eu$_2$(MoO$_4$)$_3$: a DFT + U approach

A. H. Reshak[*ab]

The spin polarized complex first-order linear optical dispersion reveals the spin-polarized electronic structure of α-Eu$_2$(MoO$_4$)$_3$. Calculation explored the influence of the generalized gradient approximation plus the Hubbard Hamiltonian (GGA + U) on the band dispersion and the energy band gap of the spin-up and spin-down and hence on the optical transitions. The appearance of Eu-4f states on the conduction band minimum of the spin-up case causes a significant influence on the ground state properties of α-Eu$_2$(MoO$_4$)$_3$. The calculated optical properties reveal that α-Eu$_2$(MoO$_4$)$_3$ possesses an indirect energy gap of about 2.2 eV (↑) and 3.2 eV (↓) in close agreement with the measured one (3.74 eV). The all-electron full potential linear augmented plane wave (FPLAPW + lo) method within GGA + U was used. We have applied U on the 4f orbitals of Eu atoms and 4d orbitals of Mo atoms to correct the ground state. We have taken a careful look at the valence band's electronic charge density distribution to visualize the charge transfer and the chemical bonding characteristics. The optical properties were calculated seeking deep insight into the electronic structure. It has been found that α-Eu$_2$(MoO$_4$)$_3$ exhibits positive uniaxial anisotropy and negative birefringence for spin-up and spin-down configurations.

1. Introduction

Molybdate crystals are characterized by specific structural characteristics, possess interesting physical and chemical properties, and the materials are widely used in modern catalysis, nanotechnology, electrochemistry and optics.[1–8] The rare-earth molybdates are of particular interest and these materials show great potential for being used for the creation of efficient laser and luminescent media.[9–15] In phosphor technology, Eu^{3+} ions doped into an appropriate host matrix provide efficient red light emission under activation in the UV spectral range.[16–21] However, under special reducing/oxidizing technological conditions, a reversible transformation Eu^{3+} ↔ Eu^{2+} is possible and europium in the host matrix can exist in these two different formal valence states.[22–24] It is well known that the spectroscopic parameters of Eu^{3+} and Eu^{2+} states are very different and the europium valence state should be precisely controlled to generate a phosphor with a predetermined combination of radiative electronic transitions. Thus, the evaluation of the optical properties and hence the electronic structure of model crystals, where Eu is in individual formal valence state, is topical.

As it is known, low-temperature monoclinic α-Eu$_2$(MoO$_4$)$_3$, space group $C2/c$, is a stable polymorphous modification at

a New Technologies – Research Centre, University of West Bohemia, Univerzitni 8, 306 14 Pilsen, Czech Republic. E-mail: maalidph@yahoo.co.uk
b Center of Excellence Geopolymer and Green Technology, School of Material Engineering, University Malaysia Perlis, 01007 Kangar, Perlis, Malaysia

room conditions and it can be taken as a representative crystal containing Eu^{3+} ions.[25–27] It should be pointed that, in the α-Eu$_2$(MoO$_4$)$_3$ structure, the europium atoms are in the position with symmetry C_1, and this avoids symmetrical constrains on the electronic parameters of Eu^{3+} ions.

The present study is aimed to investigate the optical properties to revealing the electronic structure of α-Eu$_2$(MoO$_4$)$_3$ molybdate using density functional theory (DFT) based on full-potential method. The DFT method which has proven to be one of the most accurate methods for the computation of the electronic structure of solids.[28–30]

2. Details of calculations

The experimental structural geometry of α-Eu$_2$(MoO$_4$)$_3$ compound[26] was optimized using the full potential linear augmented plane wave plus the local orbitals (FPLAPW + lo) method as implemented in WIEN2k code[31] within the generalized gradient approximation (PBE − GGA).[32] The crystal structure of α-Eu$_2$(MoO$_4$)$_3$ is shown in Fig. 1. For oxides and other highly correlated compounds, local density approximation (LDA) and GGA are known to fail to give the correct ground state.[33–35] In these systems, the electrons are highly localized. The Coulomb repulsion between the electrons in open shells should be taken into account. As there is no exchange correlation functional that can include this in an orbital independent way, a simpler approach is to add the Hubbard-like on-site repulsion to the Kohn–Sham Hamiltonian. This is known as an LDA + U or GGA + U calculations. There are different ways in
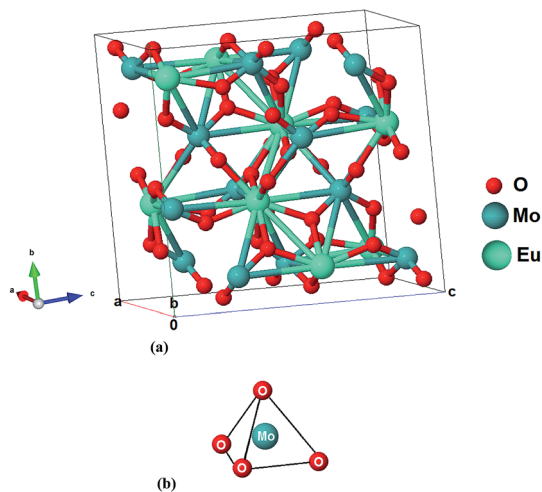
Fig. 1   (a) The crystal structure of α-$Eu_2(MoO_4)_3$; (b) MoO_4 tetrahedrons in α-$Eu_2(MoO_4)_3$.

which this can be implemented. In the present work, we used the method of Anisimov *et al.*[34] and Liechtenstein *et al.*[35] where the Coulomb (U) and exchange (J) parameters are used. From the obtained relaxed geometry the ground state properties were determined using FPLAPW + lo[32,36,37] within GGA + U (U-Hubbard Hamiltonian). We applied U on the 4f orbital of Eu atoms and the 4d orbital of Mo atoms, the U values are 0.55 Ry and 0.22 Ry respectively. As there are no experimental measurements of U for this compound, we have decided to perform calculations for various values of U and keeping the J parameter fixed at 0.05 Ry because U increases with increasing nuclear charge and valence state, whereas J is almost independent of the number of nd (nf) electrons. The main motivation for taking different U values is to find which U value gives the best fit to the measured energy gap. We take the full relativistic effects for core states and use the scalar relativistic approximation for the valence states. More details regarding the use of different values of U are found elsewhere.[38]

The potential for the construction of the basis functions inside the sphere of the muffin-tin was spherically symmetric, whereas it was constant outside the sphere. Self-consistency is obtained using 300 $\vec{k}$ points in the irreducible Brillouin zone (IBZ). The self-consistent calculations are converged since the total energy of the system is stable within 0.00001 Ry. The electronic band structure and the related properties were performed within 600 $\vec{k}$ points in the IBZ.

3.   Results and discussion

3.1.   Salient features of spin polarized electronic band structure

The spin-polarized electronic band structure of the α-$Eu_2(MoO_4)_3$ compound is calculated based on the optimized experimental structural geometry as shown in Fig. 2(a) and (b). The electronic band structure reveals that α-$Eu_2(MoO_4)_3$ compound posses indirect band gap semiconductor, as the valence band maximum (VBM) is located at the Y_0 symmetry point of the first BZ for spin-up/down, while the conduction

band minimum (CBM) is situated at the M_0 point for spin up ($\uparrow$) and at Γ point for spin down ($\downarrow$). The calculated band gaps are 2.2 eV ($\uparrow$) and 3.2 eV ($\downarrow$) in close agreement with the measured one (3.74 eV).[26] In this calculation the zero of the energy scale is taken at the top of the valence band. It was noticed that the energy gap of spin up ($\uparrow$) is noticeably lower that of spin down ($\downarrow$). That is attributed to the location of Eu-f at around 2.2 eV for the spin up ($\uparrow$) that pushes the CBM towards the Fermi level resulting in the reduced energy gap value. Whereas, for the spin down ($\downarrow$), the Eu-f states are shifted towards higher energies to be situated around 6.5 eV resulting in a shift of the CBM by around 1.0 eV towards higher energies and that increases the band gap value of spin down ($\downarrow$). It is interesting to highlight that the CBM for spin up is formed by the Eu-4f states, while for the spin-down it is originated from the Mo-d states revealing that the Eu-4f band vanished. The VBM is formed by O-p states for both spin-up/down configurations.

3.2.   Spin-polarized complex first-order linear optical dispersion

The calculated spin-polarized electronic band structure shows that the location of Eu-f state is the main factor that influence the band gap and hence the optical transitions. Analyzing the dispersion of the imaginary part of the optical dielectric function helps to gain deep insight into the electronic structure. Since these are natural outputs of band structure calculations. The calculation of the optical dielectric functions involve the energy eigenvalues and electron wave functions. Therefore, based on the calculated spin-polarized electronic band structure, we have performed calculations for the spin-polarized imaginary part of the inter-band frequency-dependent dielectric function using the expression taken from ref. 39 and 40.

$$\varepsilon_2^{ij}(\omega) = \frac{8\pi^2\hbar^2 e^2}{m^2 V} \sum_k \sum_{cv} (f_c - f_v) \frac{p_{cv}^i(k)p_{vc}^j(k)}{E_{vc}^2} \delta[E_c(k) - E_v(k) - \hbar\omega] \tag{1}$$

where m, e and $\hbar$ are the electron mass, charge and Planck's constant, respectively. f_c and f_v represent the Fermi distributions of the conduction and valence bands, respectively. The term $p_{cv}^i(k)$ denotes the momentum matrix element transition from the energy level c of the conduction band to the level v of the valence band at certain k-point in the BZ and V is the unit cell volume. The linear optical properties are calculated using the optical code implemented in the Wien2k package,[31] for more details we refer the readers to see the user guide[41] and ref. 40.

The expression no. (1), reveals that the band gap value comes in the denominator which causes the result to be very sensitive to the energy band gap value. It is well-known that the DFT leads to underestimate the energy gap value. In the DFT, by solving the Kohn–Sham equations we map an interacting many-body system to a non-interacting hypothetical system which has the same electron density. The price that we pay is the definition of a new functional that is called the exchange-correlation functional. Unfortunately, the exact form of the exchange-correlation (XC) functional is unknown. Thus, the accuracy of
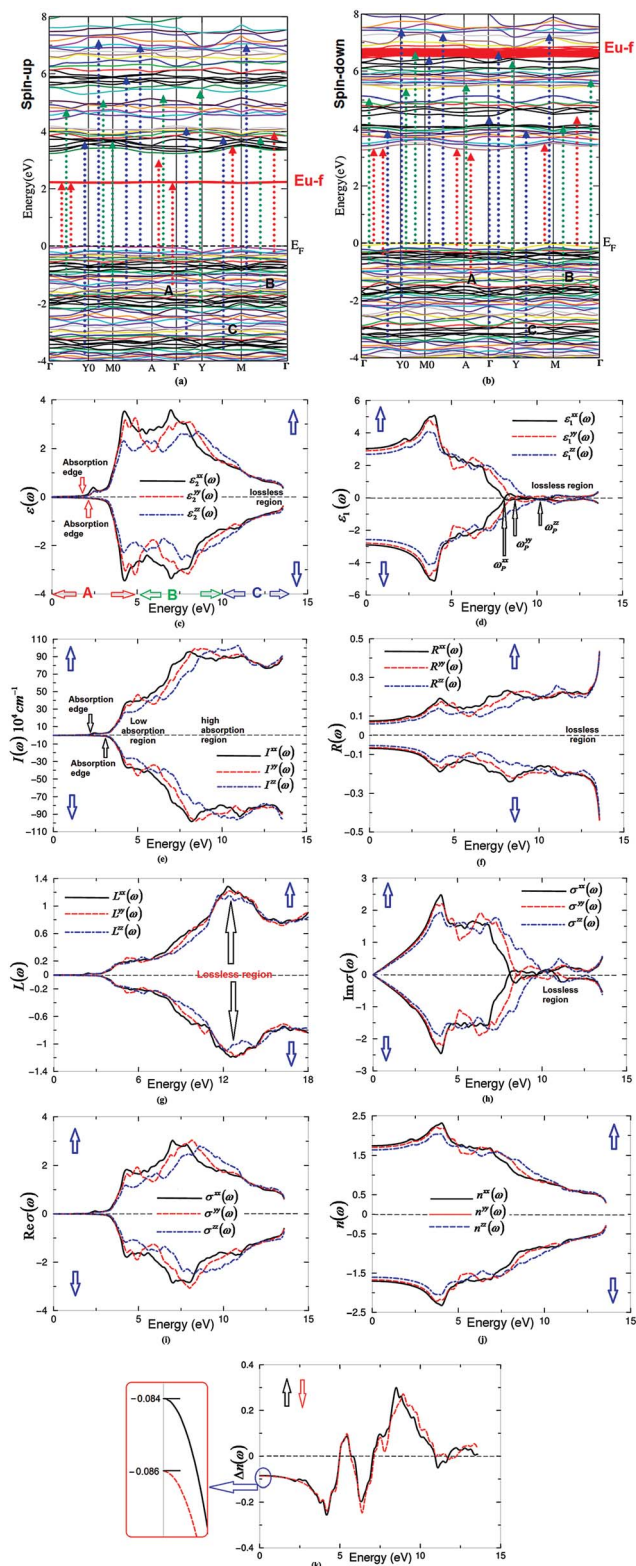
the results will be sensitive to the selection of the XC functional which can play a major role. Therefore, we have used DFT + U to calculate the spin-polarized electronic band structure and hence the spin-polarized first-order linear optical dielectric functions of α-Eu$_2$(MoO$_4$)$_3$ compound, to ascertain the influence of spin-polarization on the optical dielectric functions. Monoclinic symmetry, has several components of the dielectric tensor therefore, we will concentrate only on the major components, corresponding to an electric field perpendicular and parallel to the c-axis. These are $\varepsilon^{xx}(\omega)$, $\varepsilon^{yy}(\omega)$ and $\varepsilon^{zz}(\omega)$, which completely characterize the linear optical properties of the monoclinic system. The calculated spin-polarized imaginary part $\varepsilon_2^{xx}(\omega)(\uparrow)(\downarrow)$, $\varepsilon_2^{yy}(\omega)(\uparrow)(\downarrow)$ and $\varepsilon_2^{zz}(\omega)(\uparrow)(\downarrow)$ of the major components of the first-order linear optical dielectric functions for α-Eu$_2$(MoO$_4$)$_3$ compound along the polarization directions [100], [010] and [001] are illustrated in Fig. 2(c). It has been found that absorption edges of $\varepsilon_2^{xx}(\omega)(\uparrow)(\downarrow)$, $\varepsilon_2^{yy}(\omega)(\uparrow)(\downarrow)$ and $\varepsilon_2^{zz}(\omega)(\uparrow)(\downarrow)$ are located at 2.2 eV ($\uparrow$) and 3.2 eV ($\downarrow$). It is well-known that the edges of optical absorption (Fig. 2c) give the threshold for direct optical transitions between the VBM (Eu-6s/5p/4d, Mo-5s/4p/4d, O-2s/2p) for ($\uparrow$)($\downarrow$) and the CBM (Eu-4f) for ($\uparrow$) while Mo-4p/4d, Eu-6s/5p, O-2s/2p for ($\downarrow$) (see Fig. 2(a)–(c)). Beyond these absorption edges, a rapid increase occurs in the optical spectra to form the fundamental spectral structure of $\varepsilon_2^{xx}(\omega)(\uparrow)(\downarrow)$, $\varepsilon_2^{yy}(\omega)(\uparrow)(\downarrow)$ and $\varepsilon_2^{zz}(\omega)(\uparrow)(\downarrow)$ between 4.0 and 8.0 eV. These are due to the optical transition from Eu-6s/5p/4d, Mo-5s/4p/4d, O-2s/2p for ($\uparrow$)($\downarrow$) at the VBs to Mo-4p/4d, Eu-6s/5p, O-2s/2p bands for ($\uparrow$)($\downarrow$) at the CBs, according to the selection rules which present the maximum absorption (see Fig. 2(a)–(c)). Beyond the fundamental spectral structure, a prompt reduction occurs in the spectral structure to form the tail of $\varepsilon_2^{xx}(\omega)(\uparrow)(\downarrow)$, $\varepsilon_2^{yy}(\omega)(\uparrow)(\downarrow)$ and $\varepsilon_2^{zz}(\omega)(\uparrow)(\downarrow)$. The tail appears due to the optical transition between Eu-6s/5p/4d, Mo-5s/4p/4d, O-2s/2p) for ($\uparrow$)($\downarrow$) bands at the VBs and Eu-6s/5p/4d/4f, Mo-5s/4p, O-2s bands for ($\uparrow$)($\downarrow$) at the CBs. To identify the observed spectral structures in $\varepsilon_2^{xx}(\omega)(\uparrow)(\downarrow)$, $\varepsilon_2^{yy}(\omega)(\uparrow)(\downarrow)$ and

Fig. 2 (a) The optical transitions depicted on a generic band structure of α-Eu$_2$(MoO$_4$)$_3$ for spin-up ($\uparrow$) and (b) spin-down ($\downarrow$). For simplicity, we have labeled the optical transitions as A, B, and C. The A transitions (red color) are responsible for the optical spectral structures between (0.0–5.0) eV, the B transitions (green color) represent (5.0–10.0) eV and the C transitions (blue color) represent the spectral structures between (10.0–14.0) eV; (c) calculated $\varepsilon_2^{xx}(\omega)$ (dark solid curve-black color online), $\varepsilon_2^{yy}(\omega)$ (light dashed curve-red color online) and $\varepsilon_2^{zz}(\omega)$ (light solid curve-blue color online) spectra for spin-up/down; (d) calculated $\varepsilon_1^{xx}(\omega)$ (dark solid curve-black color online), $\varepsilon_1^{yy}(\omega)$ (light dashed curve-red color online) and $\varepsilon_1^{zz}(\omega)$ (light solid curve-blue color online) spectra for spin-up/down; (e) calculated absorption coefficient $I^{xx}(\omega)$ (dark solid curve-back color online), $I^{yy}(\omega)$ (light dashed curve-red color online) and $I^{zz}(\omega)$ (light solid curve-blue color online) spectrum. The absorption coefficient in 10^4 s^{-1}; (f) calculated $R^{xx}(\omega)$ (dark solid curve-black color online), $R^{yy}(\omega)$ (light dashed curve-red color online) and $R^{zz}(\omega)$ (light solid curve-blue color online) spectra for spin-up/down; (g) calculated $L^{xx}(\omega)$ (dark solid curve-black color online), $L^{yy}(\omega)$ (light dashed curve-red color online) and $L^{zz}(\omega)$ (light solid curve-blue color online) spectra for spin-up/down; (h) calculated Im$\sigma^{xx}(\omega)$ (dark solid curve-black color online) and Im$\sigma^{yy}(\omega)$ (light dashed curve-red color online) and Im$\sigma^{zz}(\omega)$ (light solid curve-blue color online) spectra for spin-up/down; (i) calculated Re$\sigma^{xx}(\omega)$ (dark solid curve-black color online), Re$\sigma^{yy}(\omega)$ (light dashed curve-red color online) and Re$\sigma^{zz}(\omega)$ (light solid curve-blue color online) spectra for spin-up/down; (j) calculated $n^{xx}(\omega)$ (dark solid curve-black color online), $n^{yy}(\omega)$ (light dashed curve-red color online) and $n^{zz}(\omega)$ (light solid curve-blue color online) spectra for spin-up/down; (k) calculated $\Delta n(\omega)$ (dark solid curve-black color online) and $\Delta n(\omega)$ (light dashed curve-red color online) spectra for spin-up/down.

$\varepsilon_2^{zz}(\omega)(\uparrow)(\downarrow)$ we need to look at the magnitude of the optical matrix elements following the optical selection rules. We found the observed spectral structures are corresponding to those transitions which have large optical matrix elements. We have indicated these transitions in our calculated band structure diagram. These transitions are labeled according to the peak positions in Fig. 2(c). For simplicity we have labeled the transitions in Fig. 2(a)–(c) as A, B, and C. The transitions A are responsible for the structures of $\varepsilon_2^{xx}(\omega)(\uparrow)(\downarrow)$, $\varepsilon_2^{yy}(\omega)(\uparrow)(\downarrow)$ and $\varepsilon_2^{zz}(\omega)(\uparrow)(\downarrow)$ in the energy range 0.0–5.0 eV, B (5.0–10.0) eV and C (10.0–14.0) eV. The peaks in the optical response are caused by the electric–dipole transitions between the valance and the conduction bands.

The real part of the first-order linear optical dielectric functions $\varepsilon_1^{xx}(\omega)(\uparrow)(\downarrow)$, $\varepsilon_1^{yy}(\omega)(\uparrow)(\downarrow)$ and $\varepsilon_1^{zz}(\omega)(\uparrow)(\downarrow)$ along the polarization directions [100], [010] and [001] are obtained by means of the Kramers–Kronig transformation,[39,40] as shown in Fig. 2(d). The vanishing frequency value in the dielectric function defines the static electronic dielectric constant by $\varepsilon_\infty = \varepsilon_1(0)$. These values are listed in Table 1. Furthermore, the calculated real part of the optical dielectric functions can give information about the energy gaps, since the calculated static electronic dielectric constant $\varepsilon_\infty = \varepsilon_1(0)$ is inversely related to the energy gap; this can be explained on the basis of the Penn model.[42] One of the important features of the optical spectra is the plasmon oscillations ω_p^{xx}, ω_p^{yy} and ω_p^{zz}. The plasmon oscillations are associated with inter-band transitions that occur at energies where optical spectra of $\varepsilon_1^{xx}(\omega)(\uparrow)(\downarrow)$, $\varepsilon_1^{yy}(\omega)(\uparrow)(\downarrow)$ and $\varepsilon_1^{zz}(\omega)(\uparrow)(\downarrow)$ cross zero. The values of $\omega_p^{xx}(\uparrow)(\downarrow)$, $\omega_p^{yy}(\uparrow)(\downarrow)$ and $\omega_p^{zz}(\uparrow)(\downarrow)$ are presented in Table 1. The other important feature is the uniaxial anisotropy ($\delta\varepsilon$), which can be calculated from $\varepsilon_1^{xx}(0)(\uparrow)(\downarrow)$, $\varepsilon_1^{yy}(0)(\uparrow)(\downarrow)$, $\varepsilon_1^{zz}(0)(\uparrow)(\downarrow)$ and $\varepsilon_1^{average}(0)(\uparrow)(\downarrow)$. Calculation reveals that the α-Eu$_2$(MoO$_4$)$_3$ compound exhibits positive $\delta\varepsilon$ for spin-up/down, as listed in Table 1.

The knowledge of both the real and imaginary parts of the dielectric tensor allows the calculation of important optical constants. From the calculated imaginary and real parts of the spin-polarized first-order linear optical dielectric functions we can derive the other optical properties[39,40] for instance $I(\omega)$, $R(\omega)$, $n(\omega)$ and $\sigma_2(\omega)$. The spin-polarized absorption coefficient $I^{xx}(\omega)(\uparrow)(\downarrow)$, $I^{yy}(\omega)(\uparrow)(\downarrow)$ and $I^{zz}(\omega)(\uparrow)(\downarrow)$ of α-Eu$_2$(MoO$_4$)$_3$ compound are calculated and illustrated in Fig. 2(e). The absorption spectra can be divided into three regions: the absorption edges, low absorption region and high absorption region. The absorption edges of the three tensor components along the polarization directions [100], [101] and [001] occur at 2.2 eV ($\uparrow$) and 3.2 eV ($\downarrow$) in concordance with that in Fig. 2(c).

The calculated spin-polarized optical reflectivity $R^{xx}(\omega)(\uparrow)(\downarrow)$, $R^{yy}(\omega)(\uparrow)(\downarrow)$ and $R^{zz}(\omega)(\uparrow)(\downarrow)$ of α-Eu$_2$(MoO$_4$)$_3$ compound along the polarization directions [100], [101] and [001] are shown in Fig. 2(f). The spectra reveals that at low energies, α-Eu$_2$(MoO$_4$)$_3$ compound exhibits low reflectivity. The first reflectivity maxima occurs at around 4.5 eV, followed by the a strong reflectivity maxima which is situated between 7.5 eV and 8.5 eV, confirming the occurrence of a collective plasmon resonance in concordance with our observation in Fig. 2(d). At higher energies, the region around 12.5 eV represents the lossless region.

Fig. 2(g) illustrated the calculated spin-polarized optical loss function $L^{xx}(\omega)(\uparrow)(\downarrow)$, $L^{yy}(\omega)(\uparrow)(\downarrow)$ and $L^{zz}(\omega)(\uparrow)(\downarrow)$ of α-Eu$_2$(MoO$_4$)$_3$ compound. It is clear that the loss function's peaks are initiated at the values of the plasma frequencies ω_p^{xx}, ω_p^{yy} and ω_p^{zz}. These peaks represent the parts of the optical spectra where $\varepsilon_1^{xx}(\omega)(\uparrow)(\downarrow)$, $\varepsilon_1^{yy}(\omega)(\uparrow)(\downarrow)$ and $\varepsilon_1^{zz}(\omega)(\uparrow)(\downarrow)$ cross zero.

The spin-polarized optical conductivity can be obtained from the complex first-order linear optical dielectric function following the expression $\varepsilon(\omega) = \varepsilon_1(\omega) + i\varepsilon_2(\omega) = 1 + \dfrac{4\pi i\sigma(\omega)}{\omega}$,[39,40] It consists of imaginary part (Fig. 2(h)) and real part (Fig. 2(i)); therefore, it completely characterizes the linear optical properties. The imaginary part $\sigma_2^{xx}(\omega)(\uparrow)(\downarrow)$, $\sigma_2^{yy}(\omega)(\uparrow)(\downarrow)$ and $\sigma_2^{zz}(\omega)(\uparrow)(\downarrow)$ between 0.0 and the values of ω_p^{xx}, ω_p^{yy} and ω_p^{zz} exhibit overturned features of $\varepsilon_2^{xx}(\omega)(\uparrow)(\downarrow)$, $\varepsilon_2^{yy}(\omega)(\uparrow)(\downarrow)$ and $\varepsilon_2^{zz}(\omega)(\uparrow)(\downarrow)$, whereas the real parts $\sigma_1^{xx}(\omega)(\uparrow)(\downarrow)$, $\sigma_1^{yy}(\omega)(\uparrow)(\downarrow)$ and $\sigma_1^{zz}(\omega)(\uparrow)(\downarrow)$ show similar features to those of $\varepsilon_2^{xx}(\omega)(\uparrow)(\downarrow)$, $\varepsilon_2^{yy}(\omega)(\uparrow)(\downarrow)$ and $\varepsilon_2^{zz}(\omega)(\uparrow)(\downarrow)$.

Fig. 2(j) illustrated the spin-polarized optical reflectivity spectra. The calculated values of $n^{xx}(0)(\uparrow)(\downarrow)$, $n^{yy}(0)(\uparrow)(\downarrow)$ and $n^{zz}(0)(\uparrow)(\downarrow)$ can give information about the energy gaps, since the calculated refractive indices have a relation with the energy band gap ($n = \sqrt{\varepsilon}$) (ref. 39 and 40) therefore, we can estimate the value of the energy band gap from calculated values of the refractive indices. The three components of the refractive indices show considerable anisotropy along the spectral region and hence called as birefringent. The birefringence is an important quantity to fulfils the phase-matching condition. It can be calculated from the parallel and perpendicular components of the refractive indices to the c-axis following the expression $\Delta n(\omega) = n^\perp(\omega) - n^{II}(\omega)$. Since $n^{xx}(0)(\uparrow)(\downarrow)$ almost the same as $n^{yy}(0)(\uparrow)(\downarrow)$ therefore, the average of these two components represent the parallel component $\left(n^{xx} = \dfrac{n^{xx} + n^{yy}}{2} = n^{II}(0)\right)$, whereas $n^{zz}(0) = n^\perp(0)$ represents

Table 1 Calculated $\varepsilon_1^{xx}(0)$, $\varepsilon_1^{yy}(0)$, $\varepsilon_1^{zz}(0)$, $\delta\varepsilon$, ω_p^{xx}, ω_p^{yy}, ω_p^{zz}, $n^{xx}(\omega)$, $n^{yy}(\omega)$, $n^{zz}(\omega)$ and $\Delta n(\omega)$ of α-Eu$_2$(MoO$_4$)$_3$ for spin-up ($\uparrow$) and spin-down ($\downarrow$). Where $\Delta n(\omega) = n^\perp(\omega) - n^{II}(\omega)$. Since $n^{xx}(0)(\uparrow)(\downarrow)$ almost the same as $n^{yy}(0)(\uparrow)(\downarrow)$ therefore, the average of these two components represent the parallel component $\left(n^{xx} = \dfrac{n^{xx} + n^{yy}}{2} = n^{II}(0)\right)$, whereas $n^{zz}(0) = n^\perp(0)$ represents the perpendicular component

	Spin up (↑)	Spin down (↓)
$\varepsilon_1^{xx}(0)$	3.054	2.904
$\varepsilon_1^{yy}(0)$	2.918	2.797
$\varepsilon_1^{zz}(0)$	2.700	2.566
$\delta\varepsilon$	0.098	0.103
ω_p^{xx}	8.068	8.122
ω_p^{yy}	8.666	8.530
ω_p^{zz}	9.728	10.408
$n^{II}(0)$	1.727	1.688
$n^\perp(0)$	1.643	1.602
$\Delta n(0)$	−0.084	−0.086

the perpendicular component. Fig. 2(k) represent the birefringence $\Delta n(\omega)$ of α-$Eu_2(MoO_4)_3$ compound for $(\uparrow)(\downarrow)$. The value of birefringence at zero energy $\Delta n(0)$ for $(\uparrow)(\downarrow)$ are listed in Table 1. It is clear that α-$Eu_2(MoO_4)_3$ compound posses negative birefringence for $(\uparrow)(\downarrow)$.

From above it is clear that the calculated linear optical properties show a considerable anisotropy between the three components along the polarization directions [100], [101] and [001].

We have calculated the total valence charge density distribution in two crystallographic planes for $(\uparrow)$ and $(\downarrow)$ to visualize the charge transfer and the chemical bonding characters. These are (100) and (101) as shown in Fig. 3(a)–(d) along with the tetrahedral MoO_4. The electro-negativity of Eu, Mo and O atoms according to Pauling scale are 1.2, 2.16 and 3.44, respectively. Therefore, due to the electro-negativity differences between the

atoms, some valence electrons from Eu and Mo are transferred towards O atoms as it is clear that the O atoms surrounded by uniform blue spheres (indicate the maximum charge accumulation).[43] As Mo-4d and Eu-4f orbitals have quite large hybridization with O-2p states, indicating the relatively strong covalent bonds between Mo–O and Eu–O. It is clear that the tetrahedral MoO_4 has big influence on the electronic structure, the electronic clouds (or chemical bonds) and hence on the optical properties. The tetrahedral MoO_4 groups are the main contributors to the optical anisotropy. Furthermore, the high electron density configuration and strong anisotropy of Mo–O groups indicates the main contribution of MoO_4 groups to the optical anisotropy.

It is clear that from (100) and (101) crystallographic planes all atoms are surrounding by a uniform spherical charge and Mo atoms share their outer shells with O atoms to form the
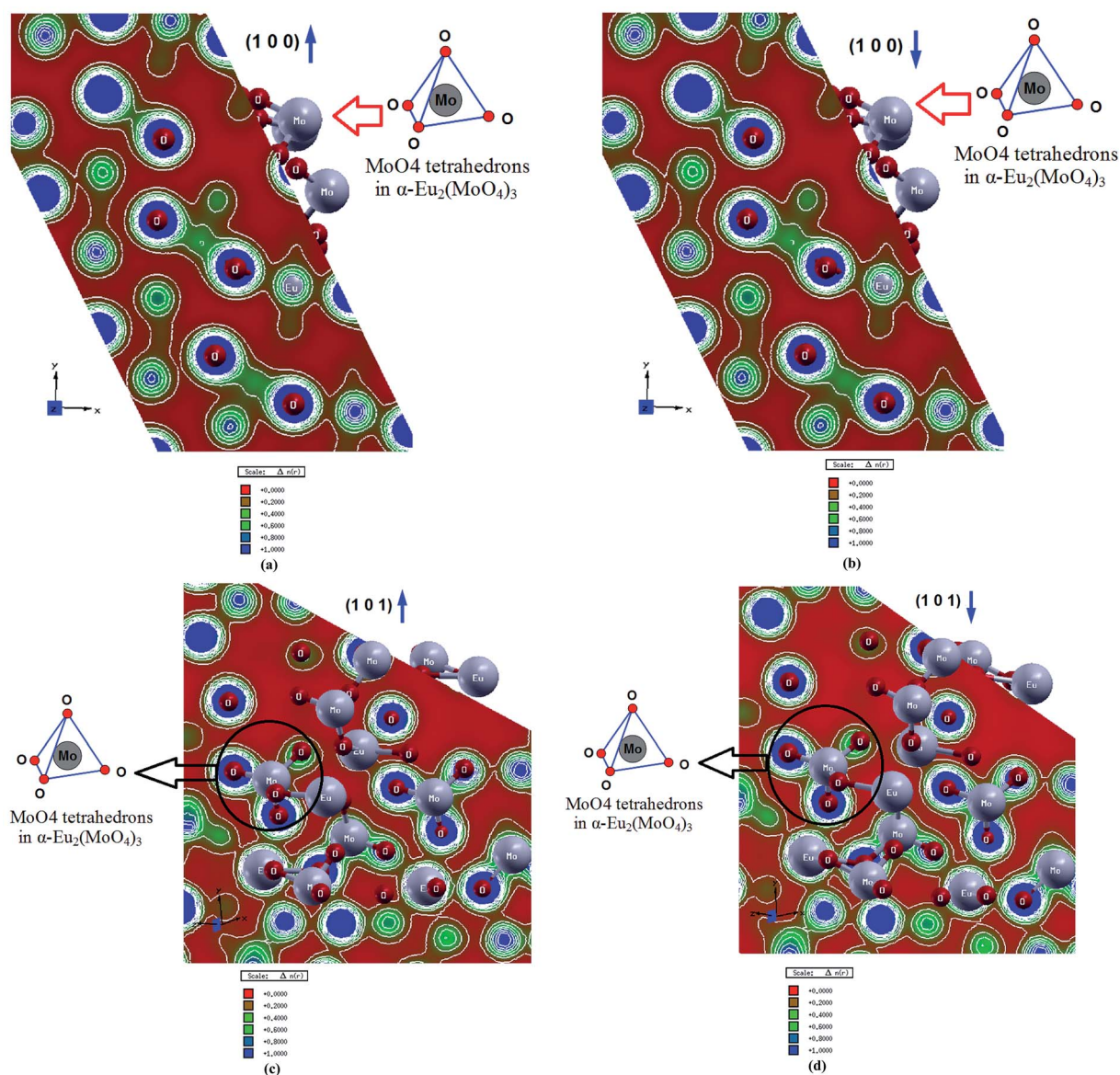

Fig. 3   Calculated electronic charge density distribution; (a) crystallographic plan (100) for spin-up case; (d) crystallographic plan (100) for spin-down case; (c) crystallographic plan (101) for spin-up case; (d) crystallographic plan (101) for spin-down case.

Table 2 Calculated main bond lengths of α-Eu$_2$(MoO$_4$)$_3$ in comparison with the measured one[26][a]

Bonds	Bond lengths (exp.) (Å)	Bond lengths (calcu.) (Å)	Bonds	Bond lengths (exp.) (Å)	Bond lengths (calcu.) (Å)
Eu–O1[i]	2.39 (2)	2.37	Eu–O6[iii]	2.50 (2)	2.49
Eu–O2	2.40 (2)	2.38	Mo1–O1	1.78 (2)	1.77
Eu–O2[ii]	2.53 (2)	2.51	Mo1–O2	1.81 (2)	1.80
Eu–O3	2.35 (2)	2.33	Mo2–O3	1.75 (2)	1.73
Eu–O4[iii]	2.43 (2)	2.42	Mo2–O4	1.73 (2)	1.71
Eu–O4[iv]	2.50 (2)	2.49	Mo2–O5[v]	1.87 (2)	1.86
Eu–O5	2.43 (3)	2.42	Mo2–O6[vi]	1.69 (2)	1.68

[a] Symmetry codes: (i) $-x + 1/2, y + 1/2, -z + 1/2$; (ii) $-x + 1/2, -y + 1/2, -z + 1$; (iii) $-x + 1, y, -z + 1/2$; (iv) $x, -y + 1, z + 1/2$; (v) $-x, y, -z + 1/2$; (vi) $-x + 1/2, -y + 1/2$.

covalent bonds. These two crystallographic planes explore the anisotropy of α-Eu$_2$(MoO$_4$)$_3$ for the spin-up (↑) and spin-down (↓). The main bond lengths were calculated and compared with the measured one[26] as shown in Table 2. Good agreement was found.

4.   Conclusions

The all-electron full potential linear augmented plane wave (FPLAPW + lo) method within the generalized gradient approximation plus the Hubbard Hamiltonian (GGA + U) were used to calculated the spin polarized complex first order linear optical dispersion to gain deep insight into the electronic structure. We have applied U on 4f orbital of Eu atoms and 4d orbital of Mo atoms. It has been found that α-Eu$_2$(MoO$_4$)$_3$ is indirect band gap semiconductor for spin-up and spin-down cases. The spin-up case exhibit smaller band gap than that obtained from the spin-down case, that is attributed to the appearance of Eu-4f states on the conduction band minimum of the spin-up case. The band structure of α-Eu$_2$(MoO$_4$)$_3$ was calculated by *ab initio* method and different results were obtained for the spin up/down configurations. The Eu-4f states are located at around 2.2 eV and -4.0 eV for spin up (↑) while they are situated at around 6.5 eV and 5.5 eV for spin down (↓) configuration. We have calculated total valence charge density distribution in (100) and (101) crystallographic planes for spin-up and spin-down cases to visualize the charge transfer and the chemical bonding characters.

Acknowledgements

References

1 F. A. Schröder, Contributions to the chemistry of Mo and W. XIV. The Mo–O bond length/bond order relationship. A systematic treatment, *Acta Crystallogr., Sect. B: Struct. Crystallogr. Cryst. Chem.*, 1975, **31**, 2294–2309.

2 V. A. Efremov, Characteristic features of the crystal chemistry of lanthanide molybdates and tungstates, *Russ. Chem. Rev.*, 1990, **59**(7), 627–642.

3 B. K. Ponomarev, Magneto-electrical properties of rare earth molybdates, *Ferroelectrics*, 2002, **280**, 95–117.

4 V. A. Isupov, Binary molybdates and tungstates of mono- and trivalent elements as possible ferroelastics and ferroelectrics, *Ferroelectrics*, 2005, **321**, 63–90.

5 I. B. Troitskaia, T. A. Gavrilova, S. A. Gromilov, D. V. Sheglov, V. V. Atuchin, R. S. Vemuri and C. V. Ramana, Growth and structural properties of α-MoO$_3$ (010) microplates with atomically flat surface, *Mater. Sci. Eng., B*, 2010, **174**(1–3), 159–163.

6 C. V. Ramana, V. V. Atuchin, H. Groult and C. M. Julien, Electrochemical properties of sputter-deposited MoO$_3$ films in lithium microbatteries, *J. Vac. Sci. Technol., A*, 2012, **30**(4), 04D105.

7 A. E. Sarapulova, B. Bazarov, T. Namsaraeva, S. Dorzhieva, J. Bazarova, V. Grossman, A. A. Bush, I. Antonyshyn, M. Schmidt, A. M. T. Bell, M. Knapp, H. Ehrenberg and J. Eckert, Possible piezoelectric materials CsMZr$_{0.5}$(MoO$_4$)$_3$ (M = Al, Sc, V, Cr, Fe, Ga, In) and CsCrTi$_{0.5}$(MoO$_4$)$_3$: structure and physical properties, *J. Phys. Chem. C*, 2014, **118**, 1763–1773.

8 V. V. Atuchin, N. V. Ivannikova, A. I. Komonov, N. V. Kuratieva, I. D. Loshkarev, N. V. Pervukhina, L. D. Pokrovsky and V. N. Shlegel, The low thermal gradient Czochralski crystal growth and microstructural properties of a Pb$_2$MoO$_5$(20−1) cleaved surface, *CrystEngComm*, 2015, **17**(24), 4512–4516.

9 A. M. Kaczmarek and R. Van Deun, Rare earth tungstate and molybdate compounds – from 0D to 3D architectures, *Chem. Soc. Rev.*, 2013, **42**, 8835–8848.

10 J. A. Enterkin, P. A. Maggard, S. Ishiwata, L. D. Marks, K. R. Poeppelmeier, M. Azuma and M. Takano, Single

crystal growth and structure of $La_4Cu_3MoO_{12}$, *J. Solid State Chem.*, 2010, **183**, 551–556.

11 V. V. Atuchin, O. D. Chimitova, T. A. Gavrilova, M. S. Molokeev, S.-J. Kim, N. V. Surovtsev and B. G. Bazarov, Synthesis, structural and vibrational properties of microcrystalline $RbNd(MoO_4)_2$, *J. Cryst. Growth*, 2011, **318**, 683–686.

12 V. V. Atuchin, V. G. Grossman, S. V. Adichtchev, N. V. Surovtsev, T. A. Gavrilova and B. G. Bazarov, Structural and vibrational properties of microcrystalline $TlM(MoO_4)_2$ (M = Nd, Pr), *Opt. Mater.*, 2012, **34**(5), 812–816.

13 Y. Yu, L. Li, Z. Lin and G. Wang, Growth, structure and optical properties of a nonlinear optical crystal α-$LaBMoO_6$, *CrystEngComm*, 2013, **15**, 5245–5249.

14 V. V. Atuchin, A. S. Aleksandrovsky, O. D. Chimitova, A. S. Krylov, M. S. Molokeev, B. G. Bazarov, J. G. Bazarova and Z. Xia, Synthesis and spectroscopic properties of multiferroic β'-$Tb_2(MoO_4)_3$, *Opt. Mater.*, 2014, **36**(10), 1631–1635.

15 C. Sung Lim, A. Aleksandrovsky, M. Molokeev, A. Oreshonkov and V. Atuchin, The modulated structure and frequency upconversion properties of $CaLa_2(MoO_4)_4$:Ho^{3+}/Yb^{3+} phosphors prepared by microwave synthesis, *Phys. Chem. Chem. Phys.*, 2015, **17**, 19278–19287.

16 P. A. Tanner, Some misconceptions concerning the electronic spectra of tri-positive europium and cerium, *Chem. Soc. Rev.*, 2013, **42**, 5090–5101.

17 A. K. Parchur, A. I. Prasad, S. B. Rai, R. Tewari, R. K. Sahu, G. S. Okram, R. A. Singh and R. S. Ningthoujam, Observation on intermediate bands in Eu^{3+}-doped YPO_4 host: Li^+ ion effect and blue to pink light emitter, *AIP Adv.*, 2012, **2**(3), 032119.

18 Y. H. Ko, S. H. Lee and J. S. Yu, Luminescence properties of europium ions-doped yttrium silicate (Y_2SiO_5:Eu^{3+}) nanocrystalline phosphors: effects of Eu^{3+} ion concentration and thermal annealing, *J. Nanosci. Nanotechnol.*, 2013, **13**, 3230–3235.

19 P. Shi, Z. Xia, M. S. Molokeev and V. V. Atuchin, Crystal chemistry and luminescence properties of red-emitting $CsGd_{1−x}Eu_x(MoO_4)_2$ solid-solution phosphors, *Dalton Trans.*, 2014, **43**, 9669–9676.

20 V. A. Morozov, B. I. Lazoryak, S. Z. Shmurak, A. P. Kiselev, O. I. Lebedev, N. Gauquelin, J. Verbeck, J. Hadermann and G. Van Tendeloo, Influence of the structure on the properties of $Na_xEu_y(MoO_4)_z$ red phosphors, *Chem. Mater.*, 2014, **26**, 3238–3248.

21 H. Ji, Z. Huang, Z. Xia, M. S. Molokeev, X. Jiang, Z. Lin and V. V. Atuchin, Comparative investigations of the crystal structure and photoluminescence property of eulytite-type $Ba_3Eu(PO_4)_3$ and $Sr_3Eu(PO_4)_3$, *Dalton Trans.*, 2015, **44**(16), 7679–7686.

22 Z. Xia, Y. Zhang, M. S. Molokeev and V. V. Atuchin, Structural and luminescence properties of yellow-emitting $NaScSi_2O_6$:Eu^{2+} phosphors: Eu^{2+} site preference analysis and generation of red emission by codoping Mn^{2+} for white-light-emitting diode applications, *J. Phys. Chem. C*, 2013, **117**, 20847–20854.

23 H. Ji, Z. Huang, Z. Xia, M. Molokeev, V. V. Atuchin, M. Fang and S. Huang, New yellow-emitting whitlockite-type structure $Sr_{1.75}Ca_{1.25}(PO_4)_2$:$Eu^{2+}$ phosphor for near-UV pumped white light-emitting devices, *Inorg. Chem.*, 2014, **53**(10), 5129–5135.

24 Z. Xia, Y. Zhang, M. S. Molokeev, V. V. Atuchin and Y. Luo, Linear structural evolution induced tunable photoluminescence in clinopyroxene solid-solution phosphors, *Sci. Rep.*, 2013, **3**, 3310.

25 K. Boulahya, M. Parras and J. M. González-Calbet, Synthesis, structural and magnetic characterization of a new scheelite related compound: $Eu_2Mo_3O_{12}$, *Eur. J. Inorg. Chem.*, 2005, 967–970.

26 V. V. Atuchin, A. S. Aleksandrovsky, O. D. Chimitova, T. A. Gavrilova, A. S. Krylov, M. S. Molokeev, A. S. Oreshonkov, B. G. Bazarov and J. G. Bazarova, Synthesis and spectroscopic properties of monoclinic α-$Eu_2(MoO_4)_3$, *J. Phys. Chem. C*, 2014, **118**, 15404–15411.

27 C. Guzmán-Afonso, S. F. León-Luis, J. A. Sans, C. González-Silgo, P. Rodríguez-Hernández, S. Radescu, A. Muñoz, J. López-Solano, D. Errandonea, F. J. Manjón, U. R. Rodríguez-Mendoza and V. Lavin, Experimental and theoretical study of α-$Eu_2(MoO_4)_3$ under compression, *J. Phys.: Condens. Matter*, 2015, **27**, 465401.

28 M. Malachowski, I. R. Kityk and B. Sahraoui, Electronic Structure and Optical Response in $Ga_xAl_{1−x}N$ Solid Alloys, *Phys. Lett. A*, 1998, **242**, 337–342.

29 I. Fuks-Janczarek, R. Miedzinski, M. G. Brik, A. Majchrowski, L. R. Jaroszewicz and I. V. Kityk, Z-scan Analysis and *Ab initio* Studies of Beta-$BaTeMo_2O_9$ Single Crystal, *Solid State Sci.*, 2014, **27**, 30–35.

30 C.-G. Ma and M. G. Brik, First Principles Studies of the Structural, Electronic and Optical Properties of $LiInSe_2$ and $LiInTe_2$ Chalcopyrite Crystals, *Solid State Commun.*, 2015, **203**, 69–74.

31 P. Blaha, K. Schwarz, G. K. H. Madsen, D. Kvasnicka and J. Luitz, *WIEN2k, An augmented plane wave plus local orbitals program for calculating crystal properties*, Vienna University of Technology, Austria, 2001.

32 J. P. Perdew, S. Burke and M. Ernzerhof, Generalized Gradient Approximation Made Simple, *Phys. Rev. Lett.*, 1996, **77**, 3865.

33 M. Cococcioni and S. D. Gironcoli, Linear response approach to the calculation of the effective interaction parameters in the LDA + U method, *Phys. Rev. B: Condens. Matter Mater. Phys.*, 2005, **71**, 035105.

34 V. I. Anisimov, I. V. Solvyev, M. A. Korotin, M. T. Czyzyk and C. A. Sawatzky, Density-functional theory and NiO photoemission spectra, *Phys. Rev. B: Condens. Matter Mater. Phys.*, 1993, **48**, 16929.

35 A. I. Liechtenstein, V. I. Anisimov and J. Zaanen, Density-functional theory and strong interactions: orbital ordering in Mott–Hubbard insulators, *Phys. Rev. B: Condens. Matter Mater. Phys.*, 1995, **52**, R5467.

36 O. K. Andersen, Linear methods in band theory, *Phys. Rev. B: Solid State*, 1975, **12**, 3060.

37 J. P. Perdew and Y. Wang, Accurate and simple analytic representation of the electron-gas correlation energy, *Phys. Rev. B: Condens. Matter Mater. Phys.*, 1992, **45**, 13244.

38 C. Guzmán-Afonso, S. F. León-Luis, J. A. Sans, C. González-Silgo, P. Rodríguez-Hernández, S. Radescu, A. Muñoz, J. López-Solano, D. Errandonea, F. J. Manjón, U. R. Rodríguez-Mendoza and V. Lavín, Experimental and theoretical study of α-Eu$_2$(MoO$_4$)$_3$ under compression, *J. Phys.: Condens. Matter*, 2015, **27**, 465401.

39 F. Bassani and G. P. Parravicini, *Electronic States and Optical Transitions In Solids*, Pergamon Press Ltd., Oxford, 1975, pp. 149–154.

40 C. Ambrosch-Draxl and J. O. Sofo, Linear optical properties of solids within the full-potential linearized augmented planewave method, *Comput. Phys. Commun.*, 2006, **175**, 1–14.

41 http://www.wien2k.at/reg_user/textbooks/usersguide.pdf.

42 D. R. Penn, Wave-Number-Dependent Dielectric Function of Semiconductors, *Phys. Rev.*, 1962, **128**, 2093–2097.

43 A. H. Reshak, S. Auluck and I. V. Kityk, Density Functional Calculations, Electronic Structure, and Optical Properties of Molybdenum Bimetallic Nitrides Pt$_2$Mo$_3$N and Pd$_2$Mo$_3$N, *J. Phys. Chem. B*, 2011, **115**, 3363–3370.